npj | precision oncology

Published in partnership with The Hormel Institute, University of Minnesota

Article

https://doi.org/10.1038/s41698-025-00869-x

Design of self-assembled micelles based on natural dual-targeting strategies and evaluation of their anti-liver cancer effects as drug delivery systems

Binbin Wang[1,4], Bai Lv[1,4], Hao Li[1,4], Jie Zhang[1], Yaning Ding[2], Jianwen Zhou[3], Ming Bu[1], Li Fan[3,5] ✉ & Cuiyan Han[1,5] ✉

Hepatocellular carcinoma (HCC) is one of the most common malignant tumors in the world and in China, Most patients are already in an advanced stage at the time of diagnosis, and the chance of complete surgical resection is lost, therefore, drug treatment is particularly important. Angelica sinensis polysaccharide (ASP) has natural liver-targeting properties, berberine (BBR) is a lipophilic cation with anticancer activities and mitochondrial-targeting properties, and honokiol (HNK) has mitochondria-dependent anticancer effects against cancer. Therefore, the aim of the present work was to synthesize Angelica sinensis polysaccharide-berberineamphiphilic polymer (ASP-SS-BBR) loaded with HNK to prepare the micelles ASP-BBR-PM@HNK to improve the hepatic targeting ability of the nanoparticles and the mitochondrial targeting ability in HCC cells and to enhance the anti-HCC effect of HNK. The findings of this study demonstrate the successful synthesis of ASP-BBR-PM@HNK, characterized by a particle size of 48.6 ± 1.13 nm. The formulation exhibits commendable stability, a sustained-release profile, and the capability for glutathione (GSH)-responsive release. ASP-BBR-PM@HNK is efficiently internalized by HepG2 cells, exhibiting the highest rate of cell inhibition. Additionally, the use of Gal and Man as receptor blockers confirmed the formulation's superior targeting capabilities, including exceptional mitochondrial targeting. Subsequent in vivo experiments employing BALB/c nude mice as a model further corroborated these experimental outcomes. This research has successfully developed an effective natural dual-targeting system, offering a novel approach for the precise treatment of liver cancer.

Hepatocellular carcinoma (HCC) represents a significant threat to human health and ranks among the five most prevalent malignant tumors, with its incidence increasing annually. The World Health Organization projects that liver cancer will result in more than 1 million deaths globally by 2030[1]. The onset of HCC imposes substantial economic and psychological burdens on patients, and the clinical prognosis for patients with HCC remains suboptimal. Current therapeutic approaches for HCC primarily include surgical resection, liver transplantation, chemotherapy, and immunotherapy. Among these options, systemic chemotherapy is considered the most effective strategy for extending patient survival. However, the systemic distribution of chemotherapeutic agents postadministration results in suboptimal drug concentrations within the target tissues and induces cytotoxic effects on nontarget organs, leading to significant toxicity and adverse side effects[2]. In recent years, the development of targeted nanodrugs has provided a new method for the treatment of liver cancer. The distinct expression of Galactose receptors (GR) and Mannose receptors (MR) on the surface of liver cancer cells presents potential targets for the selective targeting of these cells in therapeutic applications.

---

[1]College of Pharmacy, Qiqihar Medical University, Qiqihar, PR China. [2]College of Life and Health Sciences, Northeastern University, Shenyang, PR China. [3]Research Institute of Medicine and Pharmacy, Qiqihar Medical University, Qiqihar, PR China. [4]These authors contributed equally: Binbin Wang, Bai Lv, Hao Li. [5]These authors jointly supervised this work: Li Fan, Cuiyan Han.
✉e-mail: fan123456li@126.com; hcymuphar@qmu.edu.cn

THE HORMEL INSTITUTE
UNIVERSITY OF MINNESOTA

Compared with normal tissues, nanosized particles demonstrate enhanced extravasation and penetration into tumor tissues, thereby reducing off-target toxicity and improving delivery to the intended site of action. The term nanodrug delivery system (NDDS) generally refers to drug delivery systems with particle sizes ranging from 10 to 1000 nm, including liposomes, microemulsions, micelles, and nanoparticles[3]. NDDS can enhance in vivo pharmacokinetic behavior, increase drug stability and solubility, enable targeted drug delivery, control drug release, and possess increased prospects for clinical translation[4]. However, several limitations exist, including the absence of natural targeting mechanisms, elevated production costs, and additional challenges[5,6].

Polymer micelles (PM) are nanopreparations characterized by a core shell structure that forms through the self-assembly of amphiphilic block copolymers in aqueous environments. These micelles are capable of encapsulating drugs with diverse properties[7,8]. Typically, the hydrophilic segment of a PM is modified with polyethylene glycol (PEG), while polylactic acid (PLA) is frequently employed as the hydrophobic component. Standard PMs lack intrinsic targeting capabilities. Therefore, the development of naturally targeted and easily degradable PM materials holds significant promise for future applications.

Angelica sinensis polysaccharide (ASP) is a principal bioactive constituent of Angelica sinensis that has a range of health-promoting effects. Empirical evidence indicates that ASP facilitates hematopoietic regeneration and augments immunological responses. Additionally, ASP exhibits notable antitumor and antioxidant activities. A distinctive feature of ASP is its has high Galactose (Gal) density and Mannose (Man) and branched structure, appropriate spatial structure and high affinity for GR and MR, so it has natural liver targeting[9–11]. Moreover, ASP impedes the proliferation and metastasis of neoplastic cells. The incorporation of ASP as the hydrophilic segment of micelles can increase the efficacy of chemotherapy and radiation therapy, positioning it as a potential complementary treatment for cancer[12]. This strategy leverages the inherent liver-targeting properties of ASP to facilitate rapid drug delivery to hepatic sites[13]. Additionally, the superior biocompatibility and biodegradability of polysaccharides address limitations associated with traditional hydrophilic ends, such as PEG, which can induce allergic reactions and lead to accelerated clearance of particles from the bloodstream following repeated administration[14,15].

Berberine (BBR) is a natural isoquinoline alkaloid[16] that has several significant pharmacological effects, including antibacterial[17], antiviral[18], anti-inflammatory[19], and anticancer properties[20]. BBR is a lipophilic cation with an amphiphilic structure and a delocalized positive charge that selectively accumulates in the mitochondria of tumor cells[21]. Consequently, incorporating BBR into drug delivery systems can facilitate the rapid targeting of cell mitochondria to exert anticancer effects while also enhancing membrane permeability and yielding a synergistic antitumor effect[22,23].

Honokiol (HNK), an active monomer derived from natural products, has emerged as a promising candidate for antitumor therapy because of its potent pharmacological properties[24]. It has been demonstrated to have inhibitory effects on a range of cancers, including liver, breast, colon, and lung cancer[25,26]. Although HNK has mitochondria-dependent antitumor effects, its clinical application is hindered by low oral bioavailability attributed to poor water solubility[27]. Additionally, HNK may exhibit cytotoxicity in certain contexts[28], further limiting its potential for clinical use[29].

Therefore, based on the natural targeting of ASP to liver cancer cells and the natural targeting of BBR to mitochondria, HNK has mitochondria-dependent anti-tumor effects, we constructed a natural double-targeted drug delivery system. In this project, ASP functions as the hydrophilic segment, whereas lipophilic BBR constitutes the hydrophobic segment, encapsulating HNK through redox-sensitive disulfide bonds (ASP-BBR-PM@HNK). The successful synthesis of ASP-BBR-PM@HNK was validated through a comprehensive series of characterization techniques, and its dual targeting capabilities, along with its anti-HCC efficacy, were assessed using both in vivo and in vitro experimental approaches.

Results

Characterization of BBRU

The results of ^{1}H-NMR scanning of the purified BBR are shown in Fig. 1A. Compared with BBR, BBRU has a characteristic peak of -OH at 9.11 ppm,

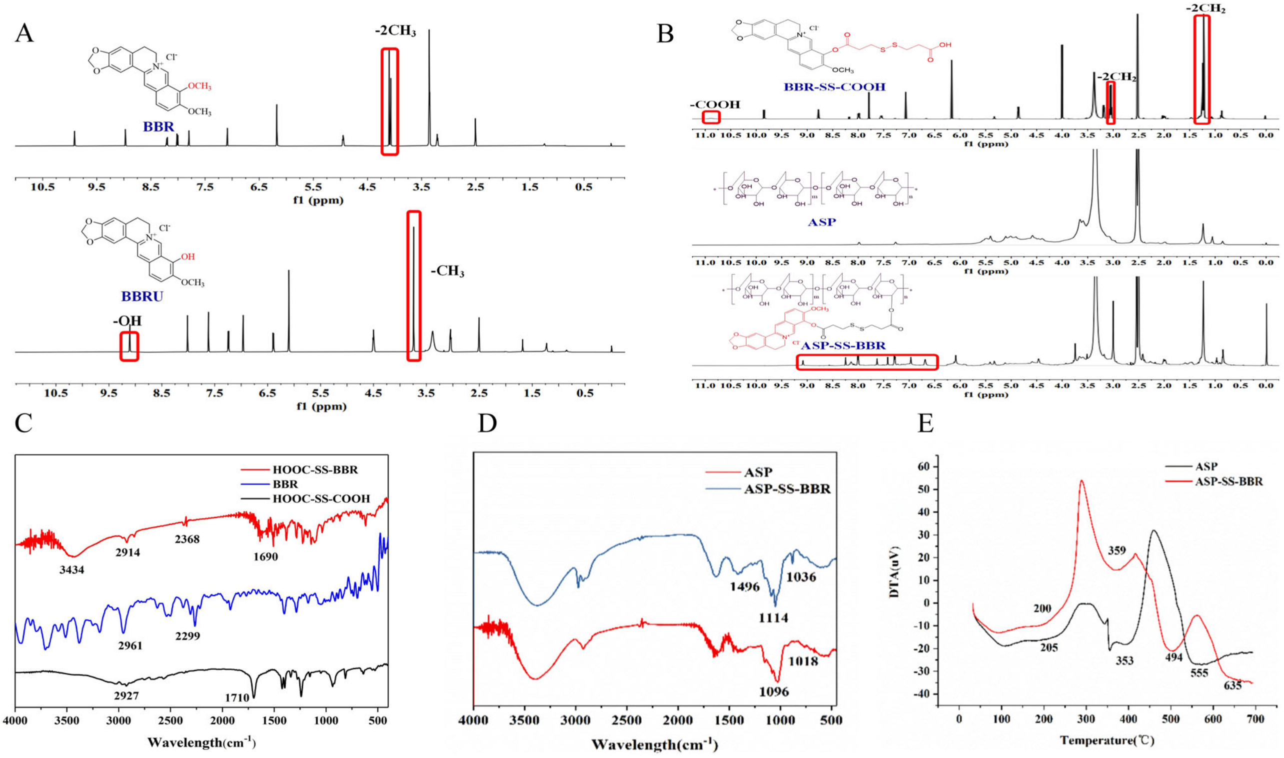

Fig. 1 | Synthesis of ASP-SS-BBR. A 1H-NMR spectra of BBR and BBRU. **B** 1H-NMR spectra of HOOC-SS-BBR, ASP, and ASP-SS-BBR. **C** FTIR spectra of BBRU, DTPA, and HOOC-SS-BBR. **D** FTIR data for ASP, ASP-SS-BBR, and HOOC-SS-BBR. **E** DTA of ASP and ASP-SS-BBR.

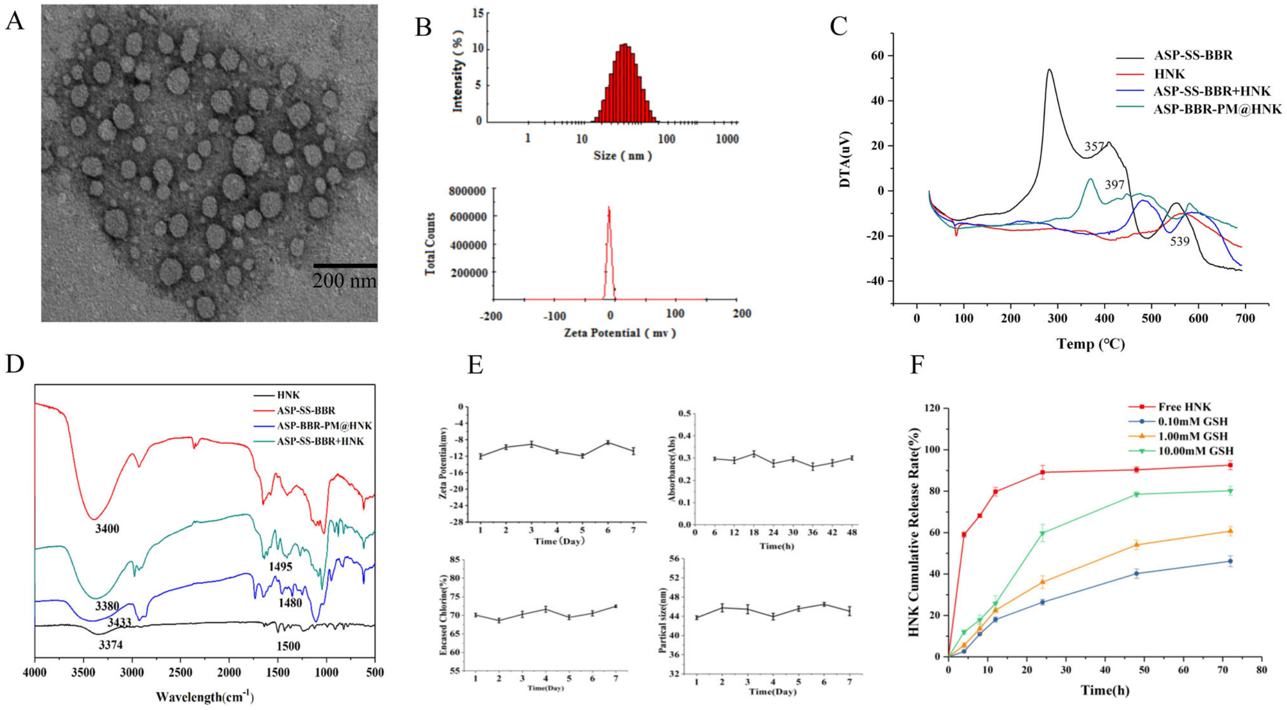

Fig. 2 | Characterization of ASP-BBR-PM@HNK. A TEM image of ASP-BBR-PM@HNK solution (×350,000). **B** Particle size distribution and potential distribution of ASP-BBR-PM@HNK. **C** DTA of ASP-SS-BBR, HNK, ASP-SS-BBR + HNK, and ASP-BBR-PM@HNK. **D** FTIR data for HNK, ASP-SS-BBR, ASP-BBR-PM@HNK, and ASP-SS-BBR + HNK. **E** Characterization of the ASP-BBR-PM@HNK stability spectrum of serum changes, particle size changes, potential changes and encapsulation rate changes. **F** HNK cumulative release curve.

and BBR has characteristic peaks of -CH_3 at 4.07 and 4.10 ppm, whereas BBRU has only one -CH_3 peak at 3.74 ppm. The characteristic peak of CH_3 indicates that a -CH_3 on BBR was transformed into -OH, which can prove that berberine was synthesized. The prepared BBRU was dark red powder with a yield of 74%.

Characterization of HOOC-SS-BBR

The obtained HOOC-SS-BBR was scanned by ^{1}H-NMR and FTIR, and the results are shown in Fig. 1B, C. The ^{1}H-NMR spectrum of HOOC-SS-BBR revealed that the characteristic peak of -COOH appeared in the low field, the characteristic peak of the four methylene groups (-CH_2-) on the substituent dithiopropionic acid appeared in the high field, and the parent characteristic peak of BBR appeared, which confirmed the successful synthesis of HOOC-SS-BBR. The FTIR spectrum of HOOC-SS-BBR revealed that the characteristic peaks of HOOC-SS-BBR at 3434 cm^{-1} and 1690 cm^{-1} were due to the dimeric structure of HOOC-SS-COOH. The stretching vibration peak of carboxylic acid-OH appeared near 2900 cm^{-1}, and the C=O stretching vibration peak appeared at approximately 1700 cm^{-1}. The characteristic peaks of HOOC-SS-BBR at 2900 cm^{-1} and 2300 cm^{-1} were due to the stretching vibration peaks of unsaturated -C-H on the benzene ring of BBR at approximately 2900 cm^{-1}. The conjugate stretching vibration of the benzene ring and -C=N peak appears on the left and right, which proves the successful synthesis of HOOC-SS-BBR. The prepared HOOC-SS-BBR was red powder with a yield of 34%.

Characterization of ASP-SS-BBR

The ^{1}H-NMR data of the prepared ASP and ASP-SS-BBR are shown in Fig. 1B. The polysaccharide had only two characteristic peaks between 6 and 10 ppm, and the characteristic peaks of BBR were mostly in the low field. The characteristic peak was masked by the characteristic peak of polysaccharides, whereas the characteristic peak of BBR was between 6-10 ppm for ASP-SS-BBR, confirming the generation of ASP-SS-BBR. As shown in Fig. 1D, ASP-SS-BBR and ASP have variable angle vibration peaks of alcohol hydroxyl groups at 1114 cm^{-1}, 1036 cm^{-1}, 1096 cm^{-1} and 1018 cm^{-1}, indicating that ASP-SS-BBR has a polysaccharide structure, and both ASP-SS-BBR and HOOC-SS-BBR have a ring breathing vibration peak of benzene at 1500 cm^{-1}, indicating the existence of a BBR structure in ASP-SS-BBR. Notably, the ASP-SS-BBR polymer was successfully constructed. Figure 1E shows that the first stage of thermal decomposition of ASP and ASP-SS-BBR is from 32–200 °C, and the main loss in this stage is water. The second stage of thermal decomposition is at 200–700 °C, indicating that the chemical bond between the two is broken. ASP has the same polysaccharide structure as ASP-SS-BBR, so there is an exothermic reaction at approximately 350 °C. However, there is one exothermic reaction at 555 °C for ASP-SS-BBR and two exothermic reactions for ASP-SS-BBR at 494 °C and 635 °C. This can be explained by the essential difference in structure between the two, and the synthesis of ASP-SS-BBR can be explained.

Characterization of ASP-BBR-PM@HNK

The TEM morphology, particle size, PDI, and zeta potential data are shown in Fig. 2A, B. ASP-BBR-PM@HNK was circular and had a uniform distribution, with a particle size of 48.6 ± 1.13 nm, PDI of 0.173 ± 0.33, zeta potential of −10.32 ± 1.26 mV, EE% of 72.87 ± 4.00%, and DL% of 8.94 ± 3.62%.

As shown in Fig. 2C, HNK, ASP-BBR-PM@HNK, and ASP-SS-BBR + HNK all have an oxidative exothermic peak at approximately 650 °C, indicating that they all contain HNK structures, and ASP-BBR-PM@HNK and ASP-SS-BBR have similar peak shapes at 397 and 357 °C, respectively, and are different from the simple physical mixing of ASP-SS-BBR + HNK, indicating that ASP-SS-BBR encapsulates HNK. ASP-SS-BBR exists in the periphery, so the exothermic peak is similar to that of ASP-SS-BBR, but after carrier consumption, the oxidative exothermic peak of HNK reappears, thus proving that ASP-BBR-PM@HNK encapsulation is successful.

As shown in Fig. 2D, HNK, ASP-SS-BBR, ASP-BBR-PM@HNK, and ASP-SS-BBR + HNK have characteristic -OH peaks at 3400 cm^{-1}, and all

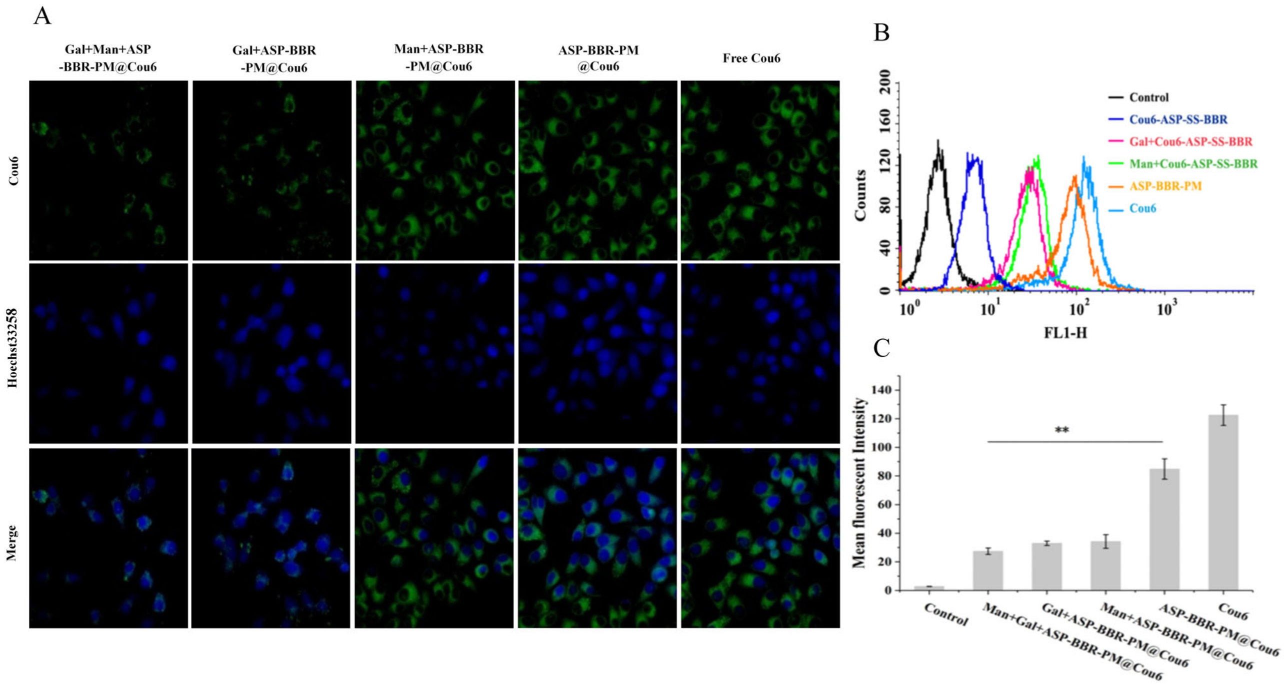

Fig. 3 | Cellular uptake in HepG2 cells. A Uptake of different Cou-6 solutions by HepG2 cells (×200). **B** Flow cytometry analysis of the uptake of Cou6 preparations in each group by HepG2 cells. **C** Quantitative analysis of Cou6 uptake via flow cytometry plots ($n = 3$, $^{**}p < 0.01$).

HNK, ASP-SS-BBR-PM@HNK and ASP-SS-BBR + HNK lines have benzene vibration peaks at 1500 cm^{-1}, and HNK and ASP-SS-BBR are mixtures. The peaks of ASP-SS-BBR + HNK and ASP-SS-BBR at approximately 2300 cm^{-1} are the conjugate telescopic vibrations of the benzene ring and -C=N, which are the characteristic peaks of BBR, but there are no such characteristic peaks at approximately 2300 cm-1 in ASP-BBR-PM@HNK, indicating that the hydrophobic side face is masked by the hydrophilic end after the formation of micelles. The characteristic peak of BBR is weakened, and HNK is contained in the carrier, so its characteristic peak is also weaker than that of the pure physical mixture.

The stability of the ASP-BBR-PM@HNK micellar solution in serum for 48 h was investigated via a microplate reader, and the storage stability of the nanoparticle size meter was measured for 7 consecutive days at 4 °C. When the particle instability increased, the absorbance value increased, and the particle size, potential, and encapsulation rate also changed greatly, as shown in Fig. 2E. The absorbance of ASP-BBR-PM@HNK within 48 h was maintained at 0.29 ± 0.09 Abs. The particle size was stable at 45.14 ± 0.67 nm within 7 days. The potential was stable at -10.46 ± 0.60 mV. The EE% was stable at 70.42 ± 1.29%, and there was no large fluctuation, indicating that the micelles had good serum and storage stability.

ASP-BBR-PM@HNK and free HNK release curves at different GSH concentrations are shown in Fig. 2F. Within the first 12 h, free HNK was released quickly, with a cumulative release rate of 79.75 ± 2.13%. The cumulative release of HNK from ASP-BBR-PM@HNK gradually increased with increasing concentrations of GSH in the release medium. When the concentrations of GSH in the release medium were 0.10 mM, 1.00 mM and 10.00 mM, the cumulative release rates of HNK after 48 h in ASP-BBR-PM@HNK were 40.2 ± 2.25%, 54.1 ± 2.27%, and 78.5 ± 1.25%, respectively. The cumulative release rates at 72 h were 46.2 ± 2.65%, 60.7 ± 2.26%, and 80.2 ± 2.21%, respectively. The results showed that ASP-BBR-PM@HNK had good GSH-sensitive drug release ability and that ASP-BBR-PM had good sustained drug release ability as a carrier. The intracellular concentration of glutathione (GSH) in tumor cells, ranging from 2 to 10 mmol/L, exceeds that of the extracellular concentration by over 1000-fold (2 to 10 μmol/L), and is also four times greater than the GSH concentration found in normal cells[35]. Notably, the concentration of GSH within the mitochondria of tumor cells is even higher. The polymer carrier ASP-SS-BBR features a hydrophilic component (ASP) and a hydrophobic component (BBR) that are interconnected by disulfide bonds, which exhibit sensitivity to GSH. The introduction of GSH facilitates the cleavage of these disulfide bonds, resulting in the release of HNK. Consequently, as the concentration of GSH increases, the release of HNK from ASP-BBR-PM@HNK is also rise.

Cellular uptake in HepG2 cells

Hoechst 33258 served as a specific nuclear dye to localize to cells, while Cou6 acted as a fluorescent probe to monitor cell uptake. The results are presented in Fig. 3A, which shows that for HepG2 cells at equal concentrations of Cou6, the uptake trend is as follows: Cou6 > ASP-BBR-PM@Cou6 > Man+ASP-BBR-PM@Cou6 > Gal+ASP-BBR-PM@Cou6 > Gal+Man+ASP-BBR-PM@Cou6. Furthermore, flow cytometry was employed to investigate the in vitro uptake ability of various preparations of Cou6 by HepG2 cells. The results are presented in Fig. 3B, C and demonstrate that the uptake size of HepG2 cells follows the order Cou6>ASP-BBR-PM@Cou6>Man+ASP-BBR-PM@Cou6>Gal+ASP-BBR-PM@Cou6>Gal + Man + ASP-BBR-PM@Cou6>blank. Moreover, the fluorescence signals of ASP-BBR-PM@Cou6 were 2.48, 2.57, and 3.09 times stronger than those of Man + ASP-BBR-PM@Cou6, Gal+ASP-Ber-PM@Cou6, and Gal + Man + ASP-BBR-PM@Cou6, respectively. This indicates that ASP-BBR-PM@HNK exhibits effective cellular uptake capabilities and can specifically target GR and MR on the surface of HepG2 cells.

Mitochondrial targeting

To investigate the ability of various Cou6 preparations to target the mitochondria of HepG2 cells, laser confocal microscopy was used with Cou6 as the fluorescent probe and MitoTracker Red as the mitochondrial localization reagent. The outcomes are shown in Fig. 4, which reveals that at the same concentration of Cou6, the mitochondrial targeting trend of HepG2 cells follows the order: ASP-BBR-PM@Cou6 > Man + ASP-BBR-PM@Cou6>Gal + ASP-BBR-PM@Cou6>Gal + Man + ASP-BBR-PM@Cou6 > Cou6. Following the interaction of HepG2 cells with ASP-BBR-PM@Cou6, the red fluorescence of ASP-BBR-PM@Cou6 was the strongest owing to the mitochondrial targeting ability of BBR. Nonetheless, owing to the blocking effect of the Gal and Man receptors, the red

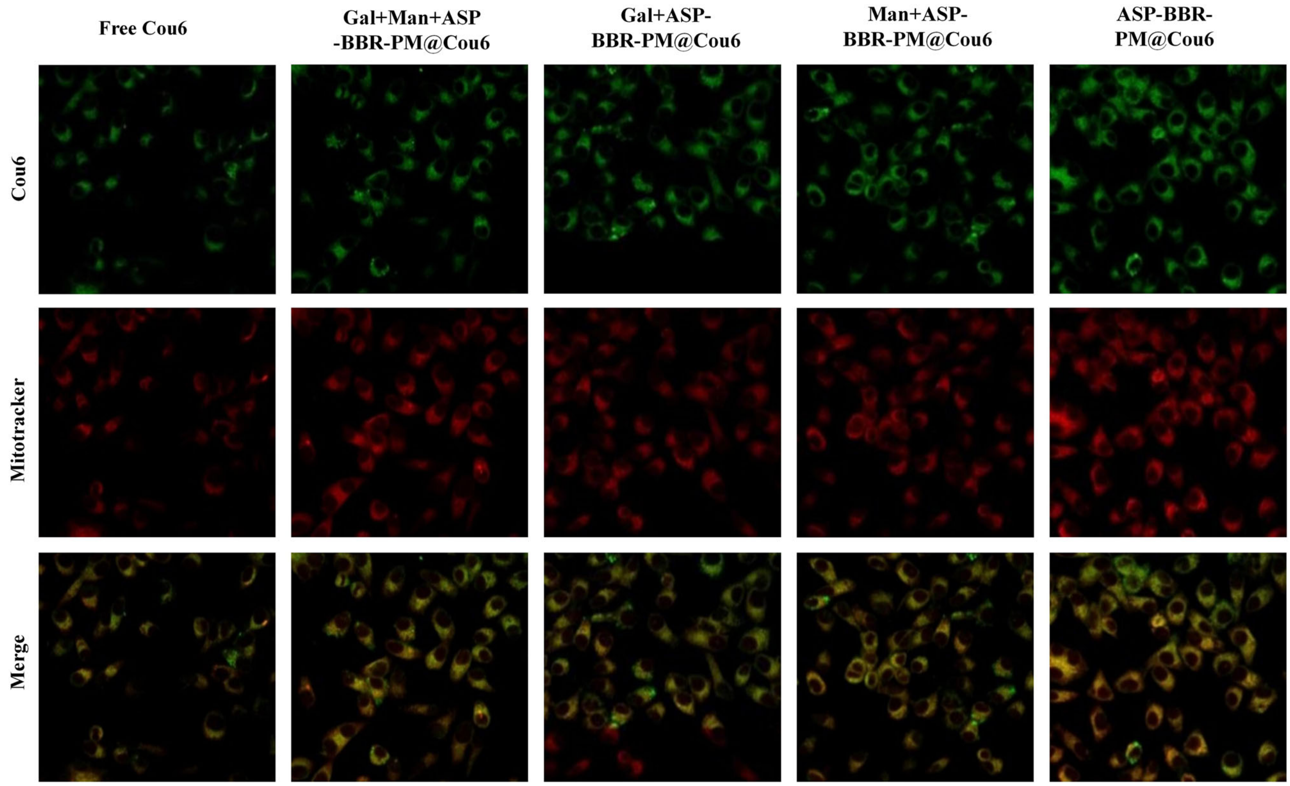

Fig. 4 | Mitochondrial targeting of HepG2 cells.

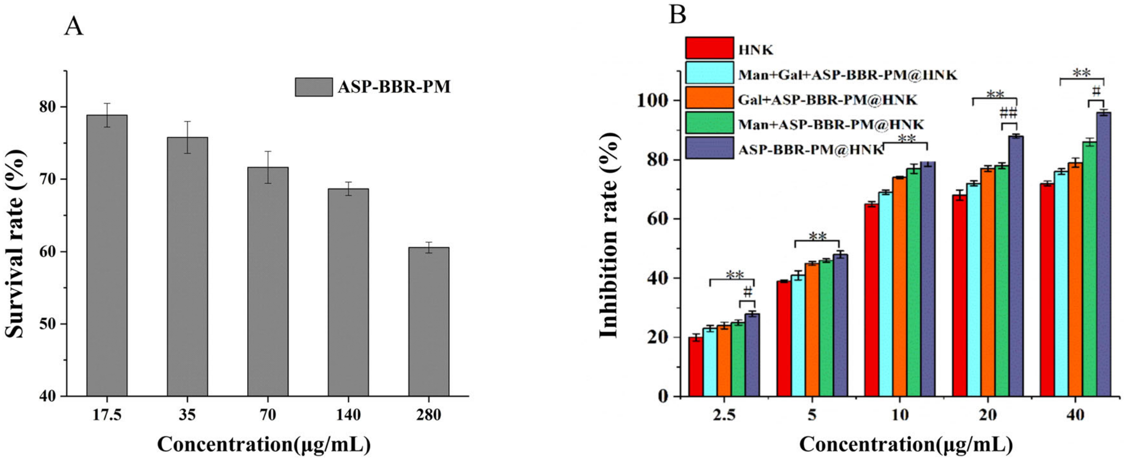

Fig. 5 | In vitro cytotoxicity studies. A Effects of blank ASP-SS-BBR carriers on the HepG2 cell survival rate ($n = 3$). **B** Inhibition rates of HepG2 cells in different drug groups ($n = 3$). Compared with the Man+ASP-BBR-PM@HNK group, $^{\#}P < 0.05$, $^{\#\#}P < 0.01$; compared with the Gal+Man+ASP-BBR-PM@HNK group, $^{**}P < 0.01$.

fluorescence of ASP-BBR-PM@Cou6 diminished after the introduction of Gal and Man. The findings demonstrated that the ASP-BBR-PM exhibited effective mitochondrial targeting capabilities and further elucidated the underlying mechanism responsible for this targeting ability.

In vitro cytotoxicity studies

Using the CCK-8 assay, the impact of ASP-BBR-PM blank micelles on the HepG2 cell survival rate was evaluated, as displayed in Fig. 5A, and the cytostatic rate of HepG2 cells was determined in different preparation groups at various concentrations of ASP-BBR-PM blank micelles, as illustrated in Fig. 5B. The inhibition rate of HepG2 cells in each sample increased with increasing mass concentration within the range of 2.5–40 μg/mL, indicating that the inhibitory effect of HNK on HepG2 cells was dose dependent. These findings suggest that increasing the concentration of blank micelles leads to a decrease in the survival rate of HepG2 cells and a certain degree of cytotoxicity. The inhibition of cell proliferation was as follows: ASP-BBR-PM@HNK > Man + ASP-BBR-PM@HNK > Gal + ASP-BBR-PM@HNK > Gal + Man + ASP-BBR-PM@HNK > free HNK. Additionally, the cytostatic rate appeared to decrease after the addition of Gal and Man, as observed through comparison. These results demonstrate that ASP-BBR-PM@HNK exhibits a significant cell inhibition rate in HepG2 cells, thereby providing further evidence of its underlying mechanism of action.

Tumor-targeting ability and mitochondrial-targeting ability of ASP-BBR-PM. To investigate the tumor-targeting ability of ASP-BBR-PM in

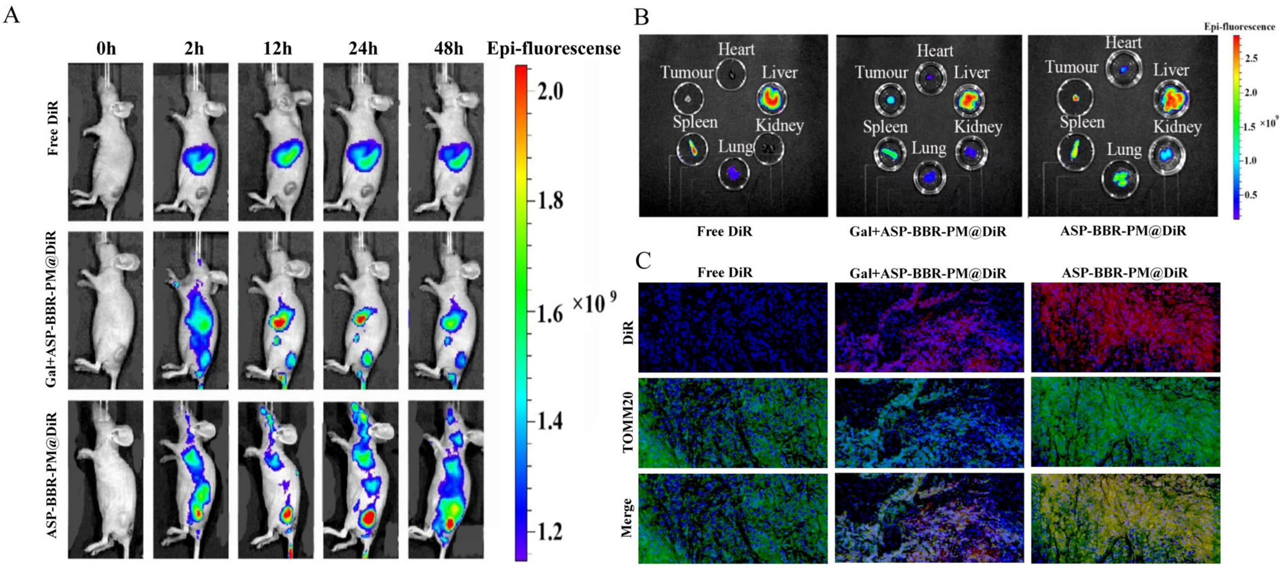

Fig. 6 | Tumor-targeting ability and mitochondrial-targeting ability of ASP-BBR-PM ($n = 5$). A Fluorescence image of BALB/c nude mice. **B** Heart, tumor, spleen, lung, kidney, and liver fluorescence images. **C** In vivo mitochondrial targeting of ASP-BBR-PM@HNK (×40).

vivo, HNK was replaced with the NIR fluorescence of DiR. After ASP-BBR-PM@DiR was intravenously injected into HepG2 tumor-bearing female BALB/c nude mice, imaging was performed via an in vivo imaging system (IVIS). The results (Fig. 6A) indicated that after intravenous injection of free DiR, significant fluorescence was observed only in the liver within 2–48 h, and no accumulation of DiR was observed at the tumor site. In contrast, in the ASP-BBR-PM@DiR group, significant fluorescent signals were observed at the tumor site as early as 2 h, and the strongest fluorescent signals were observed at 24 h. In addition, obvious fluorescent signals at the tumor sites even remained strong for up to 48 h. These findings demonstrated the excellent tumor targeting ability of ASP-BBR-PM as well as the ability of ASP-BBR-PM to accumulate at the tumor site. Finally, in the Gal + ASP-BBR-PM@DiR group, mild fluorescent signals were observed at 2 h. However, the signal was not enhanced until 48 h. The possible reason was that Gal competed for Gal receptors on hepatic carcinoma cells, resulting in weaker fluorescent signals than those in the ASP-BBR-PM@DiR group. Ex vivo tumor and tissue fluorescence images also revealed that the fluorescence intensity of the ASP-BBR-PM@DiR group tumors was the strongest after 24 h, indicating that ASP-BBR-PM could enhance drug targeting to tumors (Fig. 6B). The mitochondrial antibody TOMM20, which emits green fluorescence, was used to investigate the ability of ASP-BBR-PM to target mitochondria[36]. Figure 6C shows that no fluorescent signal in the mitochondria was observed in the free DiR group. In contrast, in the ASP-BBR-PM@DiR group, many green fluorescent signals were clustered in the mitochondria of the tumors. However, the intensity of the fluorescent signals in the Gal + ASP-BBR-PM@DiR group was lower than that in the ASP group because of the antagonistic effect of Gal on the Gal receptor. These results suggest that ASP-BBR-PM has superior mitochondrial-targeting ability in vivo.

In vivo efficacy evaluation of ASP-BBR-PM@HNK

Figure 7 shows the changes in tumor volume and weight in each group of BALB/c nude mice receiving therapy and the dissection of tumors and their regeneration after treatment ended. The results revealed that the tumor volume in each group increased with time, and compared with that in the normal saline group, the tumor volume in the ASP-BBR-PM@HNK group decreased significantly. Furthermore, in the ASP-BBR-PM@HNK group, the tumor weight was substantially reduced, and the tumor weight inhibition rate considerably increased 24 h after the last dose. These results demonstrate that ASP-BBR-PM@HNK exhibits an excellent in vivo anti-HCC effect.

Immunohistochemistry assay

To further elucidate the mechanism of apoptosis in tumor cells, the protein expression levels of Bcl-2 and CD31 in the mice were determined via immunohistochemical experiments. High expression of Bcl-2 inhibits apoptosis and accelerates cell growth, which in turn leads to tumorigenesis. Positively expressed cells in the ASP-BBR-PM@HNK group appear purple. However, via immunohistochemistry, CD31 was used to assess tumor angiogenesis, and its upregulation may indicate the extent of a rapidly growing tumor. Brown granules, indicating positive CD31 expression, were not clearly observed in the mice treated with ASP-BBR-PM@HNK. Taken together, these findings indicate that ASP-BBR-PM@HNK could significantly induce apoptosis in tumor cells, thus simultaneously increasing antitumor efficacy (Fig. 8).

Discussion

In this study, the ASP-SS-BBR polymer was synthesized by linking ASP to BBR through disulfide bonds. Its successful synthesis was confirmed via FTIR and ^{1}H-NMR scanning. The ASP-BBR-PM@HNK micelle solution was prepared through thin film hydration, resulting in a reddish-brown solution with a uniform particle size distribution, high encapsulation rate, drug load, stability, and sustained release effect in vitro. The ASP-BBR-PM@HNK demonstrates not only a high entrapment efficiency but also the capability for responsive release of glutathione (GSH), thereby exhibiting distinct advantages over previous studies in the same domain[37–39].

HepG2 cells were used as a model, and Gal+ASP-BBR-PM@HNK, Man+ASP-BBR-PM@HNK, and Gal+Man+ASP-BBR-PM@HNK were used as controls. The ASP-BBR-PM@HNK group demonstrated stronger tumor cell targeting, mitochondrial targeting, and inhibitory effects in vitro. In vitro experiments demonstrated that ASP-BBR-PM@HNK exhibits significant targeting capabilities and a high tumor cell inhibition rate, attributed to the inherent dual targeting properties of ASP-BBR-PM. The observed decrease in cell inhibition rate following the introduction of a receptor blocker provides additional support for its targeting mechanism, which is specifically designed to interact with GR and MR that are abundantly expressed on the surface of liver cancer cells. This interaction enhances the delivery of therapeutic agents to the tumor site, thereby improving efficacy. When combined with the mitochondrial targeting properties of BBR, this dual-targeting approach enhances the drug's capacity to effectively eradicate tumor cells. ASP-BBR-PM@HNK leverages the natural targeting properties of the drugs and displays superior targeting ability towards tumor cells

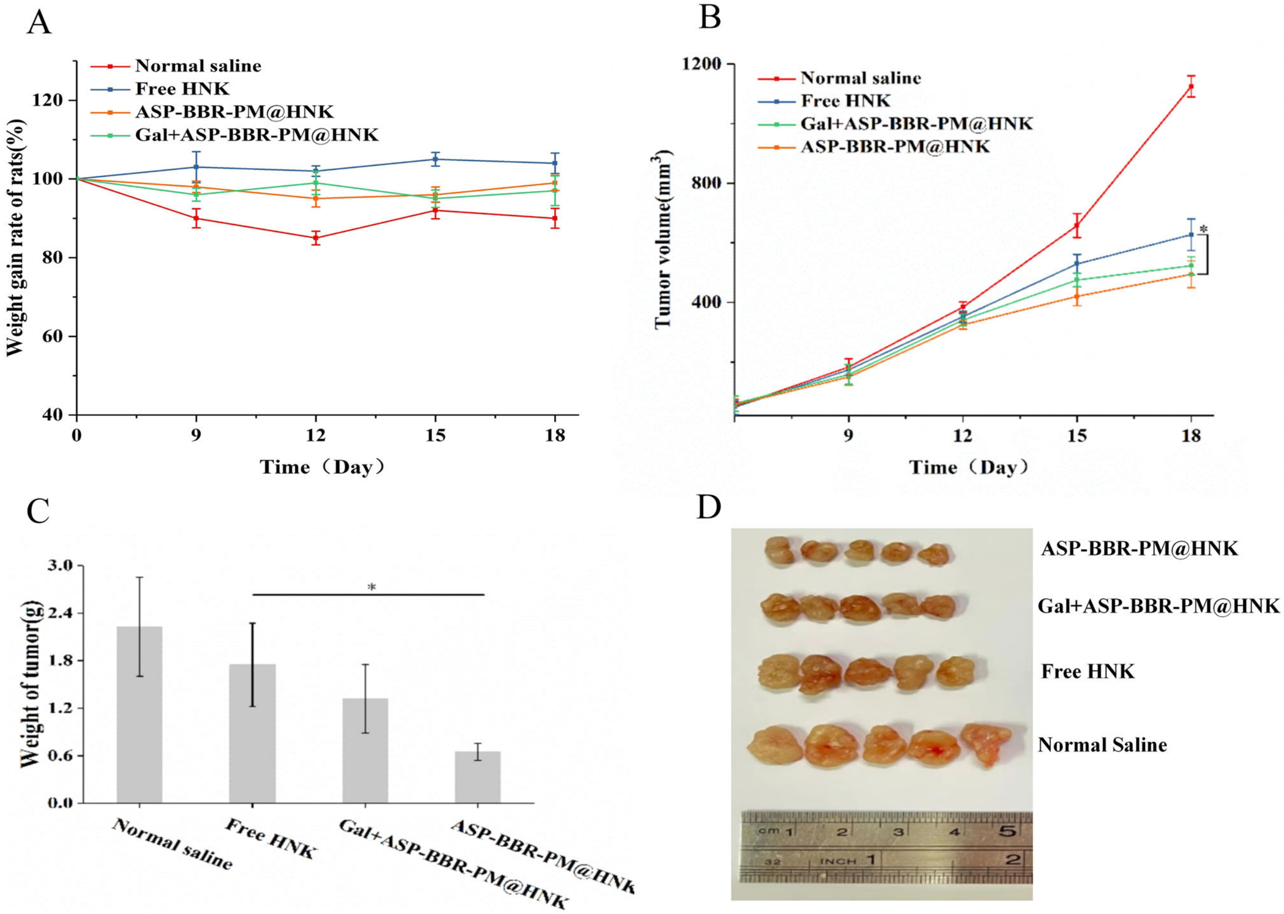

Fig. 7 | In vivo efficacy evaluation of ASP-BBR-PM@HNK. **A** Changes in the body weights of the mice in each group during drug administration (±s, $n = 5$). **B** Changes in the tumor volume of the mice in each group during administration (±s, $n = 5$). Compared with the free HNK group, $*P < 0.05$. **C** Changes in the weight of the excised tumor mass. **D** Representative photographs of dissected tumors.

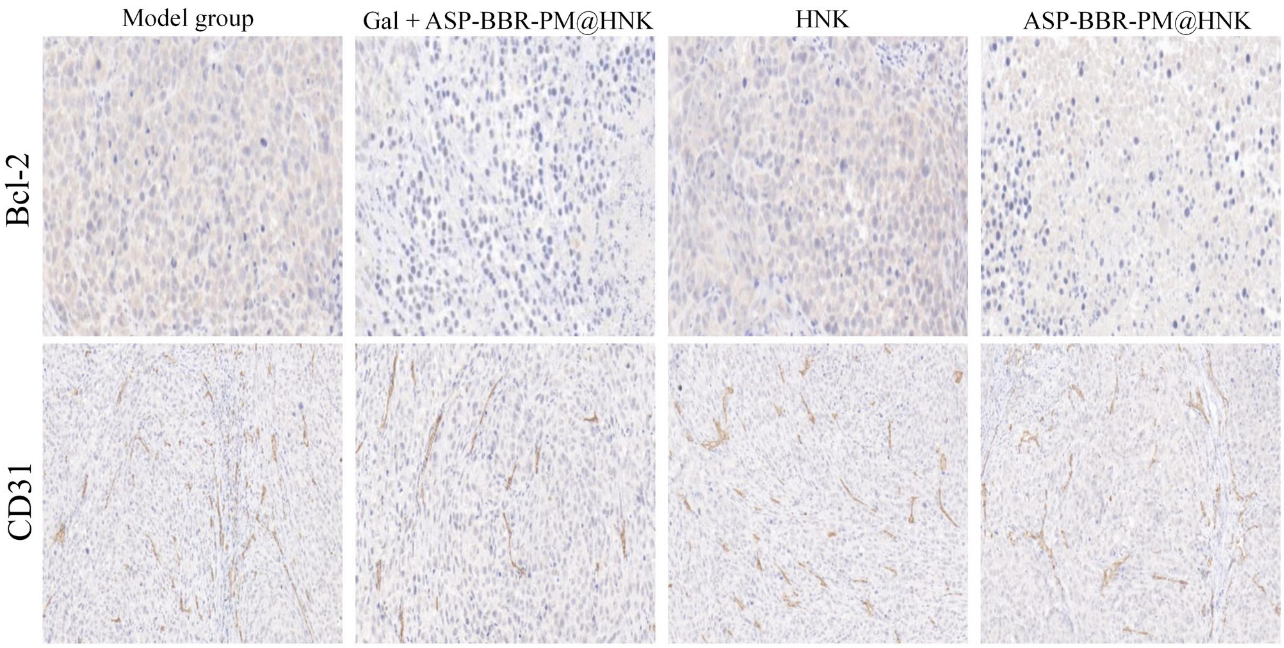

Fig. 8 | Immunohistochemistry of apoptosis in liver cancer cells.

compared to conventional micellar formulations[40,41]. Additionally, it exhibits comparable targeting capabilities to formulations with added targeting groups, while also possessing mitochondrial targeting properties[42].

A BALB/c nude mouse model was established, and Gal+ASP-BBR-PM@DiR was used as a control. ASP-BBR-PM@DiR exhibited increased liver and mitochondrial targeting in vivo. The tumor volume and weight of model mice in the ASP-BBR-PM@HNK group were significantly lower than those in the HNK and Gal+ASP-BBR-PM@HNK groups, with a substantial increase in the tumor inhibition rate, effectively suppressing tumor growth. The findings from the in vivo experiments further confirmed the targeting capability and tumor inhibitory efficacy of ASP-BBR-PM@HNK. In comparison to analogous studies[43,44], ASP-BBR-PM@HNK demonstrates significant advantages.

In this study, ASP and BBR, linked via a disulfide bond, were employed to encapsulate HNK. ASP exhibits the ability to target GR and MR on liver cancer cells, and when combined with BBR, it forms a dual-target system that demonstrates enhanced specificity compared to prior studies[45,46]. The superior targeting capability of ASP-BBR-PM facilitates precise delivery to tumor tissues following HNK loading. Furthermore, the release of ASP and BBR upon disulfide bond cleavage enhances the tumor inhibitory efficacy of ASP-BBR-PM@HNK, indicating a more pronounced anti-tumor potential relative to previous analogous studies[47,48].

The findings substantiated that ASP-BBR-PM@HNK functions as an effective adhesive polymer micelles, augmenting the liver-targeting efficacy of nanoparticles and the mitochondrial-targeting capabilities within liver cancer cells. Furthermore, it enhances the anti-liver cancer effects of HNK, indicating significant promise for clinical application.

Methods

Chemicals

ASP, BBR, anhydrous tetrahydrofuran, 3, 3-dithiodipropionic acid, 4-dimethylaminopyridine (DMAP), oxalyl chloride, triethylamine, 1-ethyl-3-(3-dimethylaminopropyl) carbodiimide hydrochloride (EDC·HCl), pyrene, reduced glutathione were all purchased from Shanghai McLean Biochemical Technology Co., Ltd. (Shanghai, China). HNK was purchased from Dalian Meilun Biotch Co., Ltd. (Dalian, China). 1,1′- Dioctadecyl-3,3,3′,3′-tetramethylindotricarbocyanine iodide (DiR), coumarin-6 (Cou6), Hoechst 33258, were all purchased from Sigma-Aldrich (Shanghai, China).

Synthesis and characterization of BBRU

Berberrubine (BBRU) was synthesized from Berberine (BBR). Briefly, BBR was placed in a vacuum drying oven at 190 °C -210 °C for 15-30 min to activate BBR's -OCH_3 to -OH. Under the polarity of dichloromethane: methanol = 4: 1, column chromatography was used to separate and purify to obtain BBRU. ^{1}H-NMR scan was performed to confirm its successful synthesis.

Synthesis and characterization of HOOC-SS-BBR

In an ice bath, 3,3-Dithiodipropionic acid (DTA) (50 mg, 0.24 mM) was dissolved in 1 mL of anhydrous tetrahydrofuran solution, rapidly dropped into oxalyl chloride (43.8 μL, 0.29 mM), and reacted for 10 min. After mixing, transfer the vial to a 35 °C oil bath and continue the reaction for 2 h. Then, the solvent was removed by rotary evaporation, BBRU (77.12 mg, 0.24 mM) was added, an appropriate amount of triethylamine was used as a catalyst, and the reaction was continued for 3 h under a 45 °C oil bath. HOOC-SS-BBR was separated and purified by column chromatography at the polarity of dichloromethane:methanol = 4:1. The prepared HOOC-SS-BBR was scanned by FTIR and ^{1}H-NMR to confirm its successful synthesis.

Synthesis and characterization of ASP-SS-BBR

Through esterification, HOOC-SS-BBR could be directly attached to ASP to form the polymer ASP-SS-BBR. Add EDC and DMAP (HOOC-SS-BBR:EDC:DMAP molar ratio = 1:1.5:1) to the anhydrous DMSO, followed by ASP. After stirring at 45 °C for 48 h, ethanol was added and centrifuged to obtain the pellet. The precipitate was washed with ethanol, tetrahydrofuran and diethyl ether, and finally lyophilized to obtain ASP-SS-BBR. The prepared ASP-SS-BBR was scanned by FTIR and ^{1}H-NMR to confirm its successful synthesis (Fig. 9).

Preparation of ASP-BBR-PM@HNK

Dissolve ASP-SS-BBR (5 mg) and HNK (1 mg) in 10 mL of methanol, thoroughly solubilize with ultrasound for 1 h, and remove organic solvents by rotary evaporation (50 °C, 0.083 MPa, 30 min) until a homogeneous film forms at the bottom of the bottle. Slowly add 5 mL of deionized water dropwise and place at the rotary evaporator for 2 h to hydrate until the membrane was completely dissolved in the deionized water. Finally, centrifuge (10000r, 10 min) to take the supernatant through the 0.22 μm filter membrane to obtain ASP-BBR-PM@HNK micellar solution.

Characterization of ASP-BBR-PM@HNK

The prepared ASP-BBR-PM@HNK was diluted into a suspension with an appropriate amount of deionized water, dropped onto a copper mesh, negatively stained with 2% phosphotungstic acid, dried naturally and observed under HT7700 transmission electron microscope. The Zetasizer

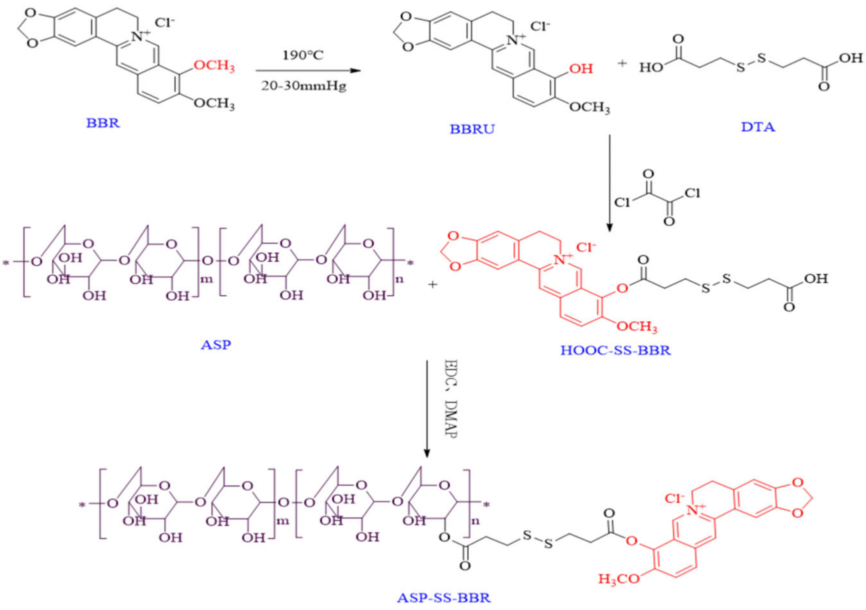

Fig. 9 | Schematic diagram of the synthesis of ASP-SS-BBR.

Nano-ZS90 nanometer particle size meter determines particle size, PDI and zeta potential. HPLC (Waters, USA. Chromatographic column: Diamonsil C_{18} (5 μm, 4.6 × 250 mm), detection wavelength: 292 nm, mobile phase: acetonitrile: water (volume ratio: 70:30), injection volume: 20 μL, column temperature: 40 °C, flow rate: 1.0 ml/min.) determined the drug load (DL%) and encapsulation rate (EE%) of ASP-BBR-PM@HNK (The formulas for DL% and EE% are as formulas (1) and (2)). Differential thermal and FTIR structure confirmation of ASP-BBR-PM@HNK. An appropriate volume of the ASP-BBR-PM@HNK solution was dispensed into a 96-well plate containing serum and incubated for 48 hours. During this period, absorbance values were recorded hourly using a microplate reader to assess serum stability. Post-incubation, the absorbance values of ASP-BBR-PM@HNK were measured at various time points using a microplate reader set to a wavelength of 490 nm. Significant changes in absorbance values would indicate particle aggregation. The ASP-BBR-PM@HNK solution stored at 4 °C was taken and the Zetasizer ZS 90 nm particle size meter continuously determined its particle size and potential value. HPLC was measured continuously for one week and its EE% change was calculated to investigate the storage stability of the sample.

$$\mathrm{EE\%} = \frac{\text{quality of HNK wrapped in micelles}}{\text{quality of the input of HNK}} \times 100\% \tag{1}$$

$$\mathrm{DL\%} = \frac{\text{quality of HNK wrapped in micelles}}{\text{quality of HNK} + \text{quality of ASP} - \text{BBR} - \text{PM}} \times 100\% \tag{2}$$

Drug release of ASP-BBR-PM@HNK

In our research, the release of HNK from ASP-BBR-PM@HNK micelles at different glutathione (GSH) concentrations were studied by the dialysis method. Put 1 mL of ASP-BBR-PM@HNK into a dialysis bag (MWCO 14000 Da). The two ends of the dialysis bag were clamped and immersed in different concentrations of GSH (0.10 mM, 1.00 mM, or 10.00 mM) in PBS (containing 0.5% Tween-80, pH 7.4), while the free HNK in the control group was set. The mixture was shaken at 100 r/min for 72 h in a constant temperature shaker at 37 °C. 1 mL samples were collected at predetermined time points (0.5, 1, 2, 4, 8, 12, 24, 48, and 72 h) and then supplemented with the same volume of fresh release medium. The sample was passed through a 0.45 μm filter membrane and injected into HPLC to calculate the percentage of cumulative release in vitro.

Cell culture

HepG2 cell line comes from the Molecular Biology Experiment Center of Qiqihar Medical University. (Qiqihar, China). HepG2 cells was cultured in Dulbecco's modified Eagle's medium (DMEM, Gibco) supplemented with 10% (v/v) fetal bovine serum (Hyclone) and antibiotics (100 U/mL penicillin and 100 U/mL streptomycin) (Hyclone) at 37 °C in a humidified atmosphere containing 5% CO2.

Cellular uptake effects

HepG2 cells were seeded into specialized plates at a density of 1×10^6 cells/wells and incubated overnight at 37 °C, in a 5% CO_2 incubator. Cou6-labeled nanoparticles were prepared using the same method employed for HNK-loaded nanoparticles. Serum-free medium containing free Cou6 or ASP-BBR-PM@Cou6 was added to the cells and incubated at 37 °C for 1 h. Additionally, a competitive inhibition experimental group was established in which excessive free Man, Gal, or Gal + Man (1 mg/mL) were added to the cells and incubated for 1 h prior to the addition of ASP-BBR-PM@Cou6. The three groups off cells were recorded as Man + ASP-BBR-PM@Cou6, Gal + ASP-BBR-PM@Cou6, and Gal + Man + ASP-BBR-PM@Cou6. The fluorescence density of each group was measured using flow cytometry[30].

In vitro mitochondrial targeting

Grouping of experiments is the same as 2.7.1. HepG2 cells were seeded in specialized plates at a density of 1×10^4 cells/well and cultured at 5% CO_2 and 37 °C for 12 h. ASP-BBR-PM@Cou6 was added under the same culture conditions for another 60 or 120 minutes. The cells were rinsed 3 times with 2 mL of PBS buffer under dark condition and then staining with the mitochondrial localization reagent Mitotracker Red (1 μM) and incubated under the same culture conditions for 25 min. After completion of the incubation, the cells were washed three more times with 2 mL of PBS buffer and the fluorescence of the cells was observed using laser confocal microscopy.

Cytotoxic assay

Digested cells were seeded in a 96-well plate at a density of 1×10^4 cells/well and cultured for 24 h. The medium was then aspirated out, and the cells with culture medium served as the control group, while free HNK, ASP-BBR-PM@HNK, Gal+ASP-BBR-PM@HNK, Man+ASP-BBR-PM@HNK, and Gal + Man + ASP-BBR-PM@HNK were tested as experimental groups. HNK mass concentrations in each experimental group were set to 2.5, 5.0, 10.0, 20.0 and 40.0 μg/mL, respectively, and 6 wells were utilized for each group. After 48 h of culture, 10 μL of CCK-8 solution was added to each well under dark conditions. The absorbance (OD) value of each well was then determined at 450 nm after 4 h to calculate the cell inhibition rate.

Experimental animals

Animal Ethical Care Committee of Qiqihar Medical University provided ethical approval for the in vivo experiments. A total of 35 BALB/c nude mice (six weeks old, 18-22 g) were purchased from the animal house colony of the Department of Chemistry. All animal experiments in this study were conducted following protocols evaluated and approved by the Ethical Committee of Qiqihar Medical University. Before the trials, the mice were allowed to acclimate for one week at the animal house facilities, where they were kept in constant environmental conditions at 22 ± 3 °C and 50 ± 5% relative humidity including a 12-hour light/dark cycle and unlimited access to regular food pellets and water. HepG2 cells were digested by pancreatic enzymes, centrifuged, and dispersed innormal saline, with a final cell suspension concentration of 1×10^7 cells/mL. 200 μL of cell suspension was injected into the left hind leg of nude mice. The growth and tumorigenesis of mice were regularly observed[31].

The type of anesthetic we use is animal grade isoflurane. The anesthesia method is gas anesthesia, using 4% concentration of isoflurane to induce anesthesia and 1% concentration of isoflurane to maintain anesthesia. Set a tumor size of 2000mm^3 as the humanitarian endpoint based on the animal Experiment Humanitarian Endpoint Evaluation Guidelines(RBT173-2018, Certification and Accreditation Industry Standards of the People's Republic of China). The euthanasia method we use is cervical dislocation after gas anesthesia with isoflurane, which is carried out by professional technicians.

In vivo targeting evaluation

DiR-labeled nanoparticles were prepared using the same method employed for HNK-loaded nanoparticles, and then injected into liver cancer model mice through the tail vein at a DiR equivalent dose of 200 μg/kg. The mice were randomly assigned to one of 3 groups of 5: free DiR, ASP-BBR-PM@DiR, or Gal + ASP-BBR-PM@DiR groups. At 0, 2, 12, 24, and 48 h after injection, the distribution of ASP-BBR-PM in vivo was observed and images were acquired using the small animal in vivo imaging system. After 24 h, the mice in each group were sacrificed, and the tumors, as well as the major organs, were dissected. Images of the isolated tumors and major organs were then captured using the imaging system.

In vivo mitochondrial targeting

The TOMM20 protein expression was identified by IHC analysis. Wax blocks P were then sectioned at a thickness of 4 μm. The paraffin sections were dewaxed in water and placed in EDTA buffer to microwave repair. They were incubated with 5% normal goat blocking serum for 20 min at room temperature. The blocked fresh serum were discarded, and the sections were incubated overnight at 4 °C with TOMM20 (1:250) in a wet chamber. The slides were then washed three times for 5 min. Fluorescent secondary antibodies were added dropwise in a circular manner and incubated for 60 min at room temperature. The section were cleaned with

PBS, slight spin-dry, and incubated with DAPI dye solution in a circle for 10 min at room temperature, protected from light. The section were then washed with PBS, slightly dried, and sealed with anti-fluorescence quenching sealant. Finally, they were framed and photographed[32].

In vivo pharmacodynamic evaluation

The liver cancer model mice were divided into a control group that received normal saline and an experimental group that received HNK, Gal + ASP-BBR-PM@HNK, or ASP-BBR-PM@HNK group with 5 mice in each group. A tail vein injection of 200 μL per dose every other day for 8 consecutive doses at a dose of 7.5 mg/kg (HNK concentration). The length and diameter of the tumors were measured using vernier calipers, and the body weight of the mice was recorded. The tumor volume was calculated using the formula (3). The mice were sacrificed on the day after the last dose, and the tumors were removed and weighed. The tumor weight suppression effect was calculated using the formula (4)[33].

$$V = 0.5 \times d_{max} \times {d_{min}}^2 \tag{3}$$

$$\text{tumor weight suppression effect} = \text{tumor weight in the experimental group} / \text{tumor weight in the control group} \times 100\% \tag{4}$$

Immunomodulatory effect studies

In order to further investigate the immune anti-tumor effect of ASP-BBR-PM@HNK, the expression levels of Bcl-2 and CD31 in mouse hepatocytes from different treatment groups were detected to evaluate the significance of inhibiting tumor growth. Four groups of mice carrying hepatoma cells (saline, HNK, Gal+ASP-BBR-PM@HNK, and ASP-BBR-PM@HNK) will be stained and sliced to determine the content of Bcl-2 and CD31 in mouse tumors[34].

Data analysis

The data collected were presented as mean ± standard deviation (SD). Statistical significance was assessed using either Student's t-test or one-way analysis of variance (ANOVA), depending on the number of groups being compared, followed by Bonferroni's multiple comparison test. A significance level of $P < 0.05$ was established.

Data availability

No datasets were generated or analysed during the current study. If need raw data related to the experiment, please contact the corresponding author.

Glossary

GR	Galactose receptor
MR	mannose receptor
PM	Polymer micelles
ASP	Angelica sinensis polysaccharide
BBR	Berberine
HNK	Honokiol
BBRU	Berberrubine
ASP-SS-BBR	The product of ASP and BBR combined by disulfide bond
ASP-BBR-PM@HNK	Polymer micelles formed by encapsulating HNK with ASP and BBR

Received: 19 December 2024; Accepted: 9 March 2025;

References

1. Singh, S. K., James, W., Lillard, R. & Singh Reversal of drug resistance by planetary ball milled (PBM) nanoparticle loaded with resveratrol and docetaxel in prostate cancer. *Cancer Lett.* **427**, 49–62 (2018).
2. Liu, S. et al. Arsenic-loaded biomimetic iron oxide nanoparticles for enhanced ferroptosis-inducing therapy of hepatocellular carcinoma. *ACS Appl. Mater. Interfaces* **15**, 6260–6273 (2023).
3. Pastucha, M., Farka, Z., Lacina, K., Mikušová, Z. & Skládal, P. Magnetic nanoparticles for smart electrochemical immunoassays: a review on recent developments. *Microchim. Acta* **186**, 312 (2019).
4. Gandhi, N. V., Deokate, U. A. & Angadi, S. S. Development of nanonized nitrendipine and its transformation into nanoparticulate oral fast dissolving drug delivery system. *AAPS PharmSciTech.* **22**, 113 (2021).
5. Qamar, Z. et al. Nano-Based drug delivery system: recent strategies for the treatment of ocular disease and future perspective. *Recent Pat. Drug Deliv. Formul.* **13**, 246–254 (2019).
6. Mu, W., Chu, Q., Liu, Y. & Zhang, N. A review on nano-based drug delivery system for cancer chemoimmunotherapy. *Nanomicro Lett.* **12**, 142 (2020).
7. Zhu, D. et al. Docetaxel (DTX)-loaded polydopamine-modified TPGS-PLA nanoparticles as a targeted drug delivery system for the treatment of liver cancer. *Acta Biomater.* **30**, 144–154 (2016).
8. Lin, M., Dai, Y., Xia, F. & Zhang, X. Advances in non-covalent crosslinked polymer micelles for biomedical applications. *Mater. Sci. Eng. C Mater. Biol. Appl.* **119**, 111626 (2021).
9. Zhang, Y. et al. Pharmacokinetics, biodistribution and receptor mediated endocytosis of a natural Angelica sinensis polysaccharide. *Artif. Cells Nanomed. Biotechnol.* **46**, 254–263 (2018).
10. Rizeq, B. R. et al. Synthesis, bioapplications, and toxicity evaluation of chitosan-based nanoparticles. *Int. J. Mol. Sci.* **20**, 5776 (2019).
11. Paurević, M. et al. Mannose ligands for mannose receptor targeting. *Int. J. Mol. Sci.* **25**, 1370 (2024).
12. Liu, X. et al. Hypoxia responsive nano-drug delivery system based on angelica polysaccharide for liver cancer therapy. *Drug Deliv.* **29**, 138–148 (2022).
13. Gonzalez, P. S. et al. Mannose impairs tumour growth and enhances chemotherapy. *Nature* **563**, 719–723 (2018).
14. Sun, B. et al. Polysaccharides as vaccine adjuvants. *Vaccine* **36**, 5226–5234 (2018).
15. Fang, L. et al. In vitro/vivo evaluation of novel mitochondrial targeting charge-reversal polysaccharide-based antitumor nanoparticle. *Carbohydr. Polym.* **234**, 115930 (2020).
16. An, R. et al. Self-assembly of fluorescent dehydroberberine enhances mitochondria-dependent antitumor efficacy. *Chemistry* **24**, 9812–9819 (2018).
17. Tuo, J. et al. Development of a novel berberine-mediated mitochondria-targeting nano-platform for drug-resistant cancer therapy. *J. Mater. Chem. B* **4**, 6856–6864 (2016).
18. Li, T. et al. Natural berberine-based chinese herb medicine assembled nanostructures with modified antibacterial application. *ACS Nano* **13**, 6770–6781 (2019).
19. Luganini, A. et al. The isoquinoline alkaloid berberine inhibits human cytomegalovirus replication by interfering with the viral Immediate Early-2 (IE2) protein transactivating activity. *Antivir. Res.* **164**, 52–60 (2019).
20. Yin, J., Hou, Y., Yin, Y. & Song, X. Selenium-coated nanostructured lipid carriers used for oral delivery of berberine to accomplish a synergic hypoglycemic effect. *Int. J. Nanomed.* **12**, 8671–8680 (2017).
21. Tan, L. et al. Dihydroberberine, a hydrogenated derivative of berberine firstly identified in Phellodendri Chinese Cortex, exerts anti-inflammatory effect via dual modulation of NF-κB and MAPK signaling pathways. *Int. Immunopharmacol.* **75**, 105802 (2019).
22. Song, J. et al. Mitochondrial targeting nanodrugs self-assembled from 9-O-octadecyl substituted berberine derivative for cancer treatment by inducing mitochondrial apoptosis pathways. *J. Control Release* **294**, 27–42 (2019).
23. Fang, L. et al. Novel mitochondrial targeting multifunctional surface charge-reversal polymeric nanoparticles for cancer treatment. *J. Biomed. Nanotechnol.* **15**, 2151–2163 (2019).

24. Wang, D. et al. Mitigation of honokiol on fluoride-induced mitochondrial oxidative stress, mitochondrial dysfunction, and cognitive deficits through activating AMPK/PGC-1α/Sirt3. *J. Hazard Mater.* **437**, 129381 (2022).
25. Munroe, M. E., Arbiser, J. L. & Bishop, G. A. Honokiol, a natural plant product, inhibits inflammatory signals and alleviates inflammatory arthritis. *J. Immunol.* **179**, 753–763 (2007).
26. Khatoon, F. et al. Pharmacological features, health benefits and clinical implications of honokiol. *J. Biomol. Struct. Dyn.* **12**, 1–23 (2022).
27. Ye, J. S. et al. SIRT3 activator honokiol ameliorates surgery/anesthesia-induced cognitive decline in mice through antioxidative stress and antiinflammatory in hippocampus. *CNS Neurosci. Ther.* **25**, 355–366 (2019).
28. Ong, C. P., Lee, W. L., Tang, Y. Q. & Yap, W. H. Honokiol: a review of its anticancer potential and mechanisms. *Cancers* **12**, 48 (2019).
29. Han, L. L. et al. Reactive oxygen species production and Bax/Bcl-2 regulation in honokiol-induced apoptosis in human hepatocellular carcinoma SMMC-7721 cells. *Environ. Toxicol. Pharm.* **28**, 97–103 (2009).
30. Li, X. et al. Polysialic acid-functionalized liposomes for efficient honokiol delivery to inhibit breast cancer growth and metastasis. *Drug Deliv.* **30**, 2181746 (2023).
31. Zhu, H., Cao, J., Cui, S., Qian, Z. & Gu, Y. Enhanced tumor targeting and antitumor efficacy via hydroxycamptothecin-encapsulated folate-modified N-succinyl-N'-octyl chitosan micelles. *J. Pharm. Sci.* **102**, 1318–1332 (2013).
32. Tang, B. et al. The ferroptosis and iron-metabolism signature robustly predicts clinical diagnosis, prognosis and immune microenvironment for hepatocellular carcinoma. *Cell Commun. Signal* **18**, 174 (2020).
33. Petersen, M. C., Vatner, D. F. & Shulman, G. I. Regulation of hepatic glucose metabolism in health and disease. *Nat. Rev. Endocrinol.* **13**, 572–587 (2017).
34. Bayer-Garner, I. B. Monkeypox virus: histologic, immunohistochemical and electron-microscopic findings. *J. Cutan. Pathol.* **32**, 28–34 (2005).
35. Fang, L. et al. Novel mitochondrial targeting charge-reversal polysaccharide hybrid shell/core nanoparticles for prolonged systemic circulation and antitumor drug delivery. *Drug Deliv.* **26**, 1125–1139 (2019).
36. Zou, A. et al. In vivo studies of octreotide-modified N-octyl-O, N-carboxymethyl chitosan micelles loaded with doxorubicin for tumor-targeted delivery. *J. Pharm. Sci.* **102**, 126–135 (2013).
37. Gou, M. et al. Self-assembled hydrophobic honokiol loaded MPEG-PCL diblock copolymer micelles. *Pharm. Res.* **26**, 2164–2173 (2009).
38. Shahid, A., Bhatt, P., Miller, A. & Sutariya, V. Honokiol-loaded methoxy poly (ethylene glycol) polycaprolactone micelles for the treatment of age-related macular degeneration. *Assay Drug Dev. Technol.* **19**, 350–360 (2021).
39. Zou, Y. et al. Synergistically enhanced antimetastasis effects by honokiol-loaded pH-sensitive polymer–doxorubicin conjugate micelles. *ACS Appl Mater. Interfaces* **22**, 18585–18600 (2018).
40. Wei, X. et al. Self-assembled honokiol-loaded micelles based on poly(ε-caprolactone)-poly(ethylene glycol)-poly(ε-caprolactone) copolymer. *Int. J. Pharm.* **369**, 170–175 (2009).
41. Dong, P. et al. Self-assembled biodegradable micelles based on star-shaped PCL-b-PEG copolymers for chemotherapeutic drug delivery. *Colloids Surf. A Physicochem. Eng. Asp.* **358**, 128–134 (2010).
42. Liu, X. et al. Hyaluronic acid-modified micelles encapsulating Gem-C12 and HNK for glioblastoma multiforme chemotherapy. *Mol. Pharm.* **15**, 1203–1214 (2018).
43. Feng, R., Deng, P., Zhou, F., Feng, S. & Song, Z. Pluronic F127-cyclodextrin conjugate micelles for encapsulation of honokiol. *J. Nanopart. Res.* **20**, 261 (2018).
44. Song, Z. et al. Oligochitosan-pluronic 127 conjugate for delivery of honokiol. *Artif. Cells Nanomed. Biotechnol.* **46**, 740–750 (2018).
45. Shi, X. et al. Anticancer effects of Honokiol via mitochondrial dysfunction are strongly enhanced by the mitochondria-targeting carrier berberine. *Med. Chem.* **63**, 11786–11800 (2020).
46. Zhang, Q. et al. Targeted delivery of honokiol by zein/hyaluronic acid core-shell nanoparticles to suppress breast cancer growth and metastasis. *Carbohydr. Polym.* **240**, 116325 (2020).
47. Xu, Y. et al. Berberine and magnolol exert cooperative effects on ulcerative colitis in mice by self-assembling into carrier-free nanostructures. *Nanobiotechnology* **22**, 538 (2024).
48. Tang, P. et al. Honokiol nanoparticles based on epigallocatechin gallate functionalized chitin to enhance therapeutic effects against liver cancer. *Int. J. Pharm.* **545**, 74–83 (2018).

Acknowledgements

This study was supported by the National Natural Science Foundation of China (No. 82174097) and the Qiqihar Science and Technology Plan, China (No. LHYD-2021001).

Author contributions

C.H. and L.F. conceived the study. B.W., B.L., and H.L. jointly completed all experiment. J.Z. and Y.D. provided guidance on the synthesis of ASP-BBR-PM. J.W.Z. and M.B. have provided great assistance in the in vivo study of ASP-BBR-PM@HNK. C.H., L.F., J.Z., and J.W.Z. supervised drug related experiments. H.L., M.B., and J.W.Z. contributed to the manuscript writing. C.H., L.F., and M.B. contributed scientific expertise and reviewed the manuscript. All the authors read and approved the manuscript.

Competing interests

The authors declare no competing interests.

Additional information

Correspondence and requests for materials should be addressed to Li Fan or Cuiyan Han.